Balanced and Unbalanced Circulations in a Primitive Equation Simulation of a Midlatitude MCC. Part II: Analysis of Balance

PETER Q. OLSSON AND WILLIAM R. COTTON

Department of Atmospheric Science, Colorado State University, Fort Collins, Colorado

(Manuscript received 7 August 1995, in final form 27 June 1996)

ABSTRACT

A nonlinear balance condition, which permits the diagnosis of both balanced divergent and nondivergent flows, is presented. This analysis approach is applied to the results of a numerical simulation of a midlatitude mesoscale convective complex (MCC) to assess the degree of balance of these and similar convective weather systems.

It is found that, to a large extent, the simulated MCC represents a highly balanced fluid system. The nondivergent component of the MCC wind field was found to be largely balanced from the time of initial convection to dissipation. Perhaps more surprisingly, the storm-induced divergent model winds are also balanced to a fair degree, though certainly less so than the nondivergent flow. Further, the balanced divergent flow makes up a significant portion of the total balanced flow in some regions of the MCC. System-scale divergence profiles of the model and balanced winds are compared and found to agree reasonably well, especially in the growth and mature stages of the MCC.

Within a stationary averaging volume enclosing the MCC, the greatest disparity between the model and balanced circulations is found in the downward vertical motion. The model downward mass flux significantly exceeds the balanced downward flux at most times during the simulation, suggesting that the process of mass adjustment due to convective heating is largely dominated by unbalanced fast-manifold processes, such as inertia–gravity waves. The unbalanced flow is found to be composed largely of divergent circulations of periodic nature (i.e., gravity waves). The appearance and characteristics of these features are found to be in good agreement with current theoretical predictions regarding the atmospheric response to convective heating and associated compensating subsidence.

The (modified) Rossby radii (λ_R) for two lowest-order gravity wave modes are calculated. The mesoscale convective vortex (MCV) within the storm is larger than λ_R for all but the gravest mode. The $\lambda_R{}^n$ for the mature storm as an ensemble also indicates a good degree of balance with $\lambda_R{}^{n=1}$ scaling similar to the MCC and larger values of n scaling smaller than the system as a whole. These λ_R values strongly suggest that this simulated MCC represents an inertially stable balanced mesoscale convective system.

1. Introduction

Much of what is considered ''meteorologically significant'' atmospheric motion can be described by a subset of the primitive equations, generically termed ''balanced models.'' These balanced models, while several in number and of varying complexity and completeness, have a common defining attribute. They neglect ''fast manifold'' behavior: those atmospheric motions, typified by gravity and acoustic waves, that have short timescales and often exhibit oscillatory behavior. While this fast manifold behavior is ubiquitous, it generally represents transient responses to changes in the energetic balance of the atmosphere. The more long-lived, ''slow-manifold'' atmospheric motions tend to be vortical in nature, especially if they occur in an environment with background rotation.

In the middle latitudes, mesoscale convective complexes (MCCs) represent an extreme case of a large-amplitude energetic perturbation to the background environment. While substantial transients are expected (and observed), a separate class of nonradiating, balanced motions also evolve. These motions, and the altered thermal structure that balances them, are conveniently contained in a single quantity, the potential vorticity (PV).

In recent years, balanced modeling has been applied to MCCs and smaller mesoscale convective systems (MCSs). Schubert et al. (1989) used a two-dimensional semigeostrophic (SG) model to study the balanced effects of an imposed heating function typical of a long squall line. Using the same model, Hertenstein and Schubert (1991) extended that study to include the heating contribution from a trailing stratiform region typical of that observed in an MCC. The results showed quite reasonable agreement with observations, especially con-

Corresponding author address: Dr. Peter Q. Olsson, Geophysical Institute, University of Alaska Fairbanks, P.O. Box 757320, Fairbanks, AK 99775-7320.
E-mail: peter.olsson@gi.alaska.edu

sidering the constraints of the two-dimensional SG model and the lack of ambient wind shear.

Raymond and Jiang (1990) used the more exact nonlinear balance (NLB) model in three dimensions to consider the effects of a PV anomaly similar to that which may be expected in a mature midlatitude MCC. They demonstrated the ability of the balanced circulations associated with such a PV distribution and background environmental shear to cause mesoscale upward motion and maintain or regenerate convection. Raymond (1992) extended his NLB model to include advection by the irrotational wind and modeled several idealized cases of forced and unforced flows with Rossby Number (R_o) of order one and also cases with no background rotation ($f=0$, $R_o \to \infty$).

A balanced model simulation of an idealized midlatitude MCS in three dimensions was performed by Jiang and Raymond (1995), who used the semibalanced model of Raymond (1992) to simulate the later (stratiform precipitation) stages of a mature MCS. An alternative approach to understanding the role balanced dynamics play in mesoscale convection was demonstrated by Davis and Weisman (1994, hereafter DW), who used PV inversion to analyze a simulated mesoscale convective vortex (MCV) produced within an idealized squall line. This use of PV inversion and the NLB equation in a diagnostic or filtering sense (as compared to a predictive model) permitted diagnosis of the balanced nondivergent component of the total flow computed by the cloud-resolving primitive equation (PE) model. DW determined that while the perturbation flow comprising the MCV was largely balanced, its formation could not be described within the constraints of balanced dynamics as defined in that paper. DW and Jiang and Raymond (1995) substantially furthered the understanding of MCSs as balanced systems, freeing the conceptual balanced model of the MCS from the quasi-axisymmetric vortex framework (e.g., Raymond and Jiang 1990) by considering the three-dimensional PV structure of the evolving system in a sheared flow.

In a companion paper Olsson and Cotton (1997, hereafter referred to as Part I) presented the results of PE simulation of a MCC, which occurred over the central United States on 23–24 June 1985. This paper, with its emphasis on the balanced dynamics of the simulation, presents a complementary analysis of that work and addresses the question: *Does the MCC represent a balanced fluid-dynamical system?* The approach used here to address this issue is similar to that of DW except that the definition of the balanced flow is extended to include the balanced or slaved secondary *divergent* circulations diagnosed from the NLB ω equation. The following section contains a discussion of the NLB equation, the associated PV approximation, and the ω equation consistent with this level of balance approximation. In section 3 results of the balanced analysis are presented. In section 4, these results are discussed and compared to current theories of adjustment to balance and compensating subsidence. The final section contains a summary of the results and conclusions.

2. Balance approximations

In the context of balanced models, the term ''balance'' generally implies a diagnostic relationship, typically between the wind and mass fields. As justified by scaling arguments, such a constraint is assumed to be approximately valid over some range of flow parameters. Incorporation of a balance approximation in the system of governing equations results in a smaller solution space. Furthermore, the balance relationship provides an invertibility condition for the PV or some similar quantity (e.g., quasigeostrophic pseudopotential vorticity, Charney and Stern 1962; the potential pseudodensity, Schubert et al. 1989). Therefore, from a given PV distribution and appropriate boundary conditions, the wind and mass fields may be determined, at least in principle. The agreement between the diagnosed ''balanced'' mass and wind fields and their observed counterparts provides a measure of the accuracy or validity of the balance approximation, that is, the degree of balance of a given fluid system at a given time. A similar comparison can be made between balanced fields and their predicted counterparts obtained from the integration of a PE model by inverting the PV computed from the model output. The latter approach is used in this study.

Quasigeostrophy (Charney 1948), the oldest and most well-known balance approximation, is based on geostrophic balance, a simple proportional relationship between the horizontal winds and pressure gradient. Several other, more general, balance approximations have been proposed and incorporated into balanced models. NLB is one of the most general of those systems that may be appropriately applied to fluids with significant rotation. Scaling arguments have been advanced to demonstrate the validity of NLB in a variety of flows (e.g., McWilliams and Gent 1980; McWilliams 1985; Raymond 1992).

To obtain the NLB condition the horizontal wind, $\mathbf{V}_h$, is decomposed into nondivergent and irrotational components. This is accomplished by defining a streamfunction, Ψ, and a velocity potential, χ, with the following properties:

$$
\begin{aligned}
\mathbf{V}_h = (u, v, 0) &= \boldsymbol{\nabla}\chi - \boldsymbol{\nabla} \times \Psi\mathbf{k} \\
\boldsymbol{\nabla}\chi = \left(\frac{\partial\chi}{\partial x}, \frac{\partial\chi}{\partial y}\right) &= (u_\chi, v_\chi), \\
\boldsymbol{\nabla} \times (-\Psi\mathbf{k}) = \left(-\frac{\partial\Psi}{\partial y}, \frac{\partial\Psi}{\partial x}\right) &= (u_\Psi, v_\Psi) \\
\nabla^2\chi = \boldsymbol{\nabla}\cdot\mathbf{V}_h &= \delta, \\
\nabla^2\Psi = \mathbf{k}\cdot\boldsymbol{\nabla} \times \mathbf{V}_h &= \zeta, \\
\boldsymbol{\nabla}\cdot(\boldsymbol{\nabla} \times \Psi\mathbf{k}) = \boldsymbol{\nabla} \times \boldsymbol{\nabla}\chi &= 0, \qquad (1)
\end{aligned}
$$

where ζ is the relative vorticity, δ the horizontal divergence, and ∇ the horizontal gradient operator. Note that this decomposition has the ambiguity that flow that is *both* nondivergent *and* irrotational may be represented by either Ψ or χ. To remove this ambiguity the following convention is used: *all flow that is both irrotational and nondivergent is represented by the streamfunction,* Ψ. *Thus, all flow represented by* χ *is strictly divergent and* (u_χ, v_χ) *shall hereafter be referred to as the divergent flow.*

The NLB approximation for frictionless flow

$$\nabla^2\Phi - \nabla\cdot(f\nabla\Psi) + -2\left[\frac{\partial^2\Psi}{\partial x^2}\frac{\partial^2\Psi}{\partial y^2} - \left(\frac{\partial^2\Psi}{\partial x\partial y}\right)^2\right] = 0, \quad (2)$$

where $\Phi = gz$ is the geopotential, is made at the level of the differentiated momentum equations and neglects δ and $\partial\delta/\partial t$ in the divergence equation. Therefore, NLB is exact for nondivergent flows, such as gradient wind balance and deformation wind fields.

To obtain an invertibility condition it is necessary to define the appropriate approximation to the exact Ertel PV:

$$q = \frac{1}{\rho}(\mathbf{Z}\cdot\nabla_3\theta) \rightarrow$$

$$q_{\text{nlb}} = -\frac{g\kappa\pi}{p(\pi)}\left[\frac{\partial^2\Psi}{\partial\pi\partial x}\frac{\partial^2\Phi}{\partial\pi\partial x} + \frac{\partial^2\Psi}{\partial\pi\partial y}\frac{\partial^2\Phi}{\partial\pi\partial y} - (\nabla_h^2\Psi + f)\frac{\partial^2\Phi}{\partial\pi^2}\right], \quad (3)$$

where the vertical coordinate is the Exner function $\pi(p) = c_p(p/p_o)^\kappa$, ρ is the density, θ the potential temperature, p the pressure, R the gas constant and c_p the specific heat capacity at constant volume; $\kappa = R/c_p$, and $\mathbf{Z}$ is the vector absolute vorticity. This approximate form of the full Ertel PV equation neglects:

- vertical shear of the horizontal divergent winds, $\mathbf{V}_\chi$, and,
- horizontal shear of the vertical velocity, a consequence of the hydrostatic approximation:

$$\theta = -\frac{\partial\Phi}{\partial\pi}. \quad (4)$$

In principle, there are an infinite number of combinations of $\Phi(x,y,\pi)$ and $\Psi(x,y,\pi)$, which satisfy a given q_{nlb} in (3). Initially, the diabatic heating perturbs the PV largely through changes in $\theta(x,y,\pi)$ (and hence to Φ through the hydrostatic approximation). However, the partitioning of PV between the vorticity and $\nabla\theta$ is uniquely defined by the NLB equation. The balance condition, in the general case, will not partition PV with the whole perturbation in the θ distribution. Evidently, the balance condition puts a significant constraint on how the system can adjust.

Equations (2) and (3) represent the invertibility condition for the NLB balance system. In simpler balance systems, such as quasigeostrophic (QG) balance, it is possible to reduce the balance equation (in that case, simply the definition of the geostrophic wind) to the functional form $\Psi = G(\Phi)$, reducing the invertibility condition to a single equation. The convergence condition for this system in this application requires that $PV > 0$ everywhere. To meet that condition, negative PV values were given a very small positive value before inversion as done in Davis and Emanuel (1991).

a. An ω *equation for the NLB system*

The PV inversion discussed above yields no representation of vertical motion. Latent heat release with its related buoyancy production is the most significant local forcing mechanism for vertical motion. Compared to other precipitating mesoscale systems, heating rates in MCSs are quite large (Houze 1989), and the divergent circulation (e.g., ascending front-to-rear and descending rear-to-front flow branches) coupled with the diabatically forced vertical motions are important factors in overall MCS organization. Clearly, any balanced theory of mesoscale convection is incomplete without some representation of these secondary circulations.

The full primitive equations allow for a rich variety of responses to such heat release. Acoustic and gravity waves, loosely termed ''fast manifold'' processes, are characterized by divergent flow and relatively fast oscillations, and act to radiate energy away from the heat source. In addition to these fast manifold modes, the primitive equations also admit a large-scale *nonradiative* or ''slow-manifold'' divergent response. It is through this subset of divergent motions that balance is achieved and maintained in a balanced model.

The ω-equation for the NLB system is formed in a manner similar to that of its QG analog. The hydrostatic vertical vorticity equation

$$\frac{\partial\zeta}{\partial t} + \mathbf{V}_\Psi\cdot\nabla(\zeta+f) = -\mathbf{v}_\chi\cdot\nabla(\zeta+f) - \omega\frac{\partial\zeta}{\partial\pi} - \delta(\zeta+f) + \left(\frac{\partial\omega}{\partial y}\frac{\partial u}{\partial\pi} - \frac{\partial\omega}{\partial x}\frac{\partial v}{\partial\pi}\right), \quad (5)$$

(a) (b) (c) (d) (e)

indicates that local changes in the (relative) vorticity may be brought about by horizontal advection of absolute vorticity by (a) the nondivergent wind, and (b) the divergent wind, (c) vertical advection of relative vorticity, (d) horizontal convergence, and (e) tilting of horizontal vorticity into (or away from) the vertical.

Casting the continuity equation in terms of the velocity potential, χ

$$\pi^{-\mu}\frac{\partial}{\partial\pi}(\pi^{\mu}\omega) = -\nabla^2\chi = -\delta, \tag{6}$$

where $\mu = 1/\kappa - 1$, indicates that for any nontrivial $\omega(\pi)$, divergent flows must be considered. Therefore, terms of $O(\chi)$ must be retained to diagnose nontrivial secondary circulations. For the vorticity equation (5), the only approximation involves neglecting the tilting of the divergent horizontal winds in (e):

$$\left(\frac{\partial\omega}{\partial y}\frac{\partial u}{\partial\pi} - \frac{\partial\omega}{\partial x}\frac{\partial v}{\partial\pi}\right) \approx \left(\frac{\partial\omega}{\partial y}\frac{\partial u_{\Psi}}{\partial\pi} - \frac{\partial\omega}{\partial x}\frac{\partial v_{\Psi}}{\partial\pi}\right) + \left(\frac{\partial\omega}{\partial v}\frac{\partial u_{\chi}}{\partial\pi} - \frac{\partial\omega}{\partial x}\frac{\partial v_{\chi}}{\partial\pi}\right); \tag{7}$$

the last term within parentheses $(\cdots) \rightarrow 0$, while the exact form of the thermodynamic equation

$$\frac{\partial\theta}{\partial t} + \mathbf{V}_h\cdot\nabla\theta + \omega\frac{\partial\theta}{\partial\pi} = Q, \tag{8}$$

with Q being the diabatic warming rate, is retained.

By combining ∇^2 (8) $-\ \partial^2/\partial t\partial\pi$ (2) $-\ f\partial/\partial\pi$ (balanced vorticity equation), the NLB omega equation is obtained:

$$\left(f\eta\frac{\partial}{\partial\pi}\left(\pi^{-\mu}\frac{\partial\Psi}{\partial\pi}(\pi^{\mu}\omega)\right) + \nabla^2(\sigma\omega)\right) - \left[f\frac{\partial}{\partial\pi}\left(\frac{\partial^2\Psi}{\partial x\partial y}\frac{\partial\omega}{\partial x} + \frac{\partial^2\Psi}{\partial x\partial y}\frac{\partial\omega}{\partial y}\right) - \left(f\frac{\partial\eta}{\partial\pi}\frac{\mu}{\pi} + \frac{\partial^2\Psi}{\partial\pi^2}\right)\omega\right] = \left[\nabla^2(\mathbf{V}_h\cdot\nabla\theta) + f\frac{\partial}{\partial\pi}(\mathbf{V}_h\cdot\nabla\eta)\right] + \left[-\beta\frac{\partial^2\Psi}{\partial x\partial y\partial t} - \frac{\partial^2}{\partial\pi\partial t}J(t) - \nabla^2Q(t)\right], \tag{9}$$

where the term *J(t)* is the Jacobian term in square braces in (2), η is the vertical absolute vorticity, $\beta = \partial f/\partial y$, and $\sigma = \partial^2\Phi/\partial\pi^2 = -\partial\theta/\partial\pi$ is a measure of static stability.

The continuity equation (6) and the NLB ω equation (9) represent a coupled system in ω and χ, the vertical and horizontal components of the balanced divergent wind. Similar to the coupled system in Φ and Ψ, a solution $[\omega(x,y,\pi), \chi(x,y,\pi)]$, can in principle be found that simultaneously satisfies these equations and accompanying boundary conditions. The ω equation describes how, through a great variety of simultaneous interactions, the divergent part of the flow adjusts with the PV and balance equation. The group of terms in (9), which are functions of $\mathbf{V}_h$, the *total* horizontal wind (and hence functions of χ), adjust the differential horizontal advection of vorticity and θ with the spatial distribution of ω. The continuity equation simultaneously maintains the conservation of mass as a function of the balanced horizontal divergent flow and the balanced vertical motion.

The terms within the last pair of square brackets in (9) are functions of time, and determine how the vertical motion is related to

- the spatially varying coriolis torque interacting with time-varying sheared zonal flow,
- time-varying vertically sheared nondivergent ageostrophic flow, and
- the spatial distribution of the diabatic warming rate.

In our diagnostic analysis of the numerical simulation, this last term (diabatic warming rate) was frequently quite large in regions where precipitation was occurring and typically dominated the ω forcing there.

Including a divergent component to the definition of the ''balanced'' wind is somewhat of a departure from conventional terminology. However, the nonradiating or ''slaved'' component of the divergent winds diagnosable in a nonlinear balance model play an important role in advection (Raymond 1992) and other dynamical processes. In light of the preceding discussion of the role that the balanced divergent flow and associated vertical motion play in achieving and maintaining balance, the authors feel that the term ''slaved'' can be misleading and prefer the term ''balanced'' divergent flow.

The two sets of equations outlined here completely define the three-dimensional balanced flow (both nondivergent and divergent) through Ψ, χ, and ω, and the balanced mass field through Φ. From these quantities, all the other relevant balanced dynamical properties of the fluid system can be deduced. Solution of these equation systems is outlined in appendix A and a description of the analysis grid, that is, the data volume upon which the PV inversion is performed, is given in appendix B.

At this point it is worthwhile to consider the potential shortcomings of this balance system in the context of the MCC. As discussed in Part I, several studies have found significant production of horizontal vorticity near the top of the low-level cold pool or gravity current commonly found preceding the leading line of convection in a maturing squall line or MCC. This cold outflow is typically divergent in nature and therefore projects largely on $\mathbf{V}_{\chi}$. Such horizontal vorticity may be tilted vertically by convective updrafts, this mechanism being instrumental in the development of some simulated MCVs (e.g., DW). As is discussed by DW and can be seen in (3), however, *it is precisely this vorticity that is not included in* q_{nlb}. The NLB vorticity equation also neglects this tilting as a source term, as seen in (7).

The above discussion would suggest that, for systems where tilting of storm-generated horizontal vorticity due to vertical shear of the *divergent* horizontal winds is instrumental in MCV production, a prognostic model based on NLB would indeed fail to evolve an MCV correctly. This is much less of a problem in the diagnostic application of NLB here since the error caused

TABLE 1. Summary of definitions of the various two-dimensional wind fields used in the discussion of the balanced analysis. See Table 1 for a definition of ''divergent'' and ''nondivergent'' in terms of the velocity potential χ and the streamfunction Ψ.

COMPONENTS OF VECTOR WINDS		
$\mathbf{V}_u = \mathbf{V}_m - \mathbf{V}_b$ $\mathbf{V}_m = \mathbf{V}_{m\Psi} + \mathbf{V}_{m\chi}$	$\mathbf{V}_{u\chi} = \mathbf{V}_{m\chi} - \mathbf{V}_{b\chi}$ $\mathbf{V}_b = \mathbf{V}_{b\Psi} + \mathbf{V}_{b\chi}$	$\mathbf{V}_{u\Psi} = \mathbf{V}_{m\Psi} - \mathbf{V}_{b\Psi}$ $\mathbf{V}_u = \mathbf{V}_{u\Psi} + \mathbf{V}_{u\chi}$
	$\mathbf{V}_b$	
$\mathbf{V}_m$ *model wind*	*balanced wind*	$\mathbf{V}_u$ *unbalanced wind*
$\mathbf{V}_{m\Psi}$ *model nondiv. wind*	$\mathbf{V}_{b\Psi}$ *balanced nondiv. wind*	$\mathbf{V}_{u\Psi}$ *unbal. nondiv. wind*
$\mathbf{V}_{m\chi}$ *model diverg. wind*	$\mathbf{V}_{b\chi}$ *balanced diverg. wind*	$\mathbf{V}_{u\chi}$ *unbal. diverg. wind*

by systematic neglect of $\mathbf{V}_\chi$ in q_{nlb} does not accumulate over several hours.

b. Definitions of balanced winds and related quantities

For the purpose of discussing the results of the balanced analysis, it is useful to define several wind fields. It is understood in the ensuing discussion that the vector winds are the horizontal winds, unless otherwise stated.

Vector field decomposition can be achieved in a number of different and useful (and probably confusing!) ways. The main interest here is in the balanced ($\mathbf{V}_b$) and unbalanced ($\mathbf{V}_u$) winds, where $\mathbf{V}_b$ is the sum of the balanced nondivergent and divergent components ($\mathbf{V}_{b\Psi}$ and $\mathbf{V}_{b\chi}$) as derived from the balanced analysis. Similar to the definition of the ageostrophic winds in the context of geostrophic balance, the (nonlinearly) unbalanced $\mathbf{V}_u$ is defined as the residual

$$\mathbf{V}_u = \mathbf{V}_m - \mathbf{V}_b. \tag{10}$$

The sum of $\mathbf{V}_u$ and $\mathbf{V}_b$ constitutes the complete, two-dimensional vector wind field ($\mathbf{V}_m$), as produced in the model. For the sake of intercomparison, it is helpful to compute the nondivergent and divergent components of the model winds. This is achieved by computing the vertical vorticity and divergence from the model data, and solving the Poisson equations defining the vorticity and divergence in terms of Ψ and χ, respectively. The sum of the decomposed winds, $\mathbf{V}_{m\Psi} + \mathbf{V}_{m\chi}$, is found to agree well with the model winds $\mathbf{V}_m$. The same approach as in (10) is then used to define the unbalanced nondivergent winds, $\mathbf{V}_{u\Psi}$, and unbalanced divergent winds, $\mathbf{V}_{u\chi}$. Table 1 contains a summary of these definitions.

In a like manner to (10), an unbalanced vertical velocity (ω_u) in the Exner function vertical coordinate system may be defined

$$\omega_u = \omega_m - \omega_b, \tag{11}$$

where ω_b satisfies both the continuity equation (6) for the balanced velocity potential χ_b, and the NLB omega equation (9).

3. Results of the balanced analysis

As shown in Part I, the first convection associated with the simulated MCC initiated around 2000 UTC 23 June 1985 (designated 23/2000) along a quasi-stationary front in central Iowa. Over the next few hours, convection developed along and south of the front in Iowa and SE Nebraska (see Fig. 6 in Part 1 for an overview of the observed and simulated storm movement and location). By 24/0000 the storm had achieved MCC status, and an MCV had formed at the eastern end of the E–W oriented convective line in SE Iowa. The MCC slowly propagated to the south, and by 24/0600 the dissipating storm extended across central Missouri westward into east-central Kansas. During the mature and dissipation stages of the MCC, a second, smaller MCV developed in far eastern Kansas. At the end of the simulation (24/1200), the stratiform cloud shield was dissipating, but a strong remnant PV anomaly still existed in the middle troposphere.

Figure 1a shows midtropospheric $\mathbf{V}_m$ just before the first convection occurred. Figure 1b shows $\mathbf{V}_u$, the unbalanced component of the model winds both at 23/1900. (Note: the wind vector scale difference between panels, with the maximum model winds about 29 m s^{-1} and the maximum unbalanced wind magnitude about 1.5 m s^{-1}.) Only in a few locations does the unbalanced wind exceed a few percent of the model wind field. A similar result is found at other analysis levels. Before the onset of convection, the balance approximation is evidently quite accurate.

Figures 2a and 2b show vector plots of storm relative $\mathbf{V}_m$ and $\mathbf{V}_b$ (the balanced winds), respectively, after about 3 h of convection. The MCV circulation in south-central Iowa appears clearly in both plots. The MCV signature in $\mathbf{V}_b$ is not surprising, since, to maintain temporal coherence, this strong long-lived vortical circulation (Part I) requires a state of near-cyclostrophic balance (a limiting case of nonlinear balance) in order to maintain temporal coherence. Overall, the winds agree quite well, though there are some differences. The major difference between $\mathbf{V}_m$ and $\mathbf{V}_b$ is due to the unbalanced divergent winds, $\mathbf{V}_{u\chi}$, which typically comprise over 80% of $\mathbf{V}_u$ at this level.

Another feature of interest evident in Fig. 2 is the anticyclonic turning of $\mathbf{V}_m$, NNE of the MCV, which is not captured in $\mathbf{V}_b$. Recall that the PV was filtered previous to inversion to ensure that the convergence condition for the Φ, Ψ solver, PV > 0 was met. In Part I it was shown that narrow bands of negative PV were generated to the north of the convective elements. The

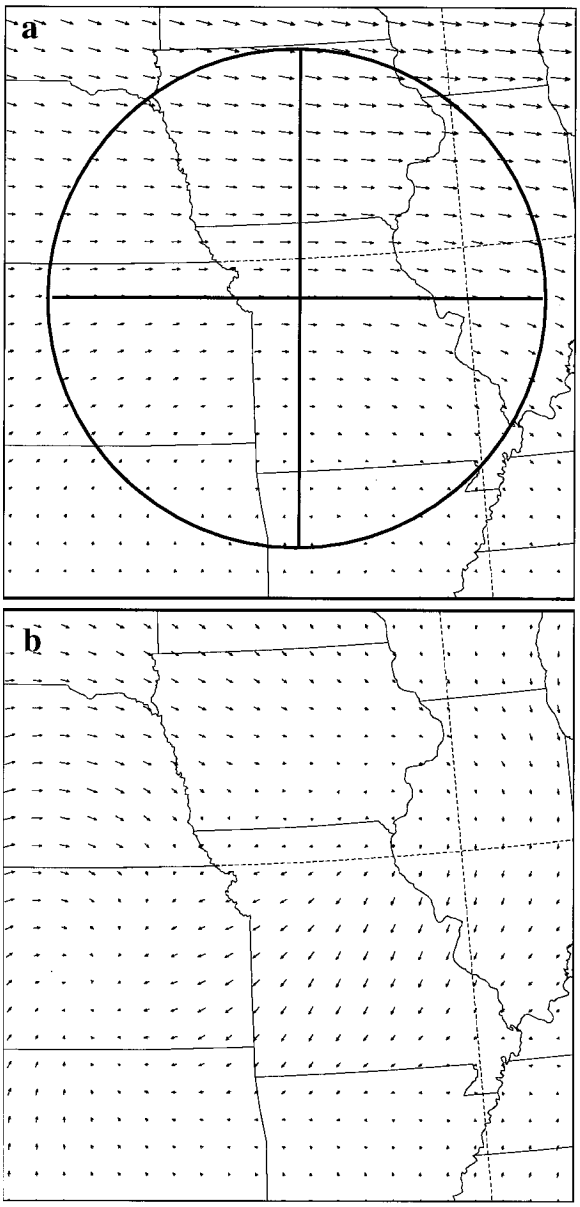

FIG. 1. (a) The model winds at 23/1900 on the 535-mb pressure level. The maximum wind vector represents a speed of 29 m s^{-1}. (b) The unbalanced winds at the same time and level. The maximum wind vector represents a speed of 1.5 m s^{-1}. For comparison, the scaling between a and b is 10:1 (a vector in panel a would be 10 times larger in panel b). The ring in Fig. 1a shows the horizontal location of the averaging domain discussed later.

filtering process by necessity caused these regions to be given very weak positive values of PV. This results in a local biasing of the PV inversion solution toward positive vorticity and represents a fundamental weakness of the balanced model paradigm. However, since the PV inversion in a sense represents a double integration, it acts as a smoothing operator and mitigates the effects of PV filtering, especially if the regions of negative PV are relatively confined as is the case here.

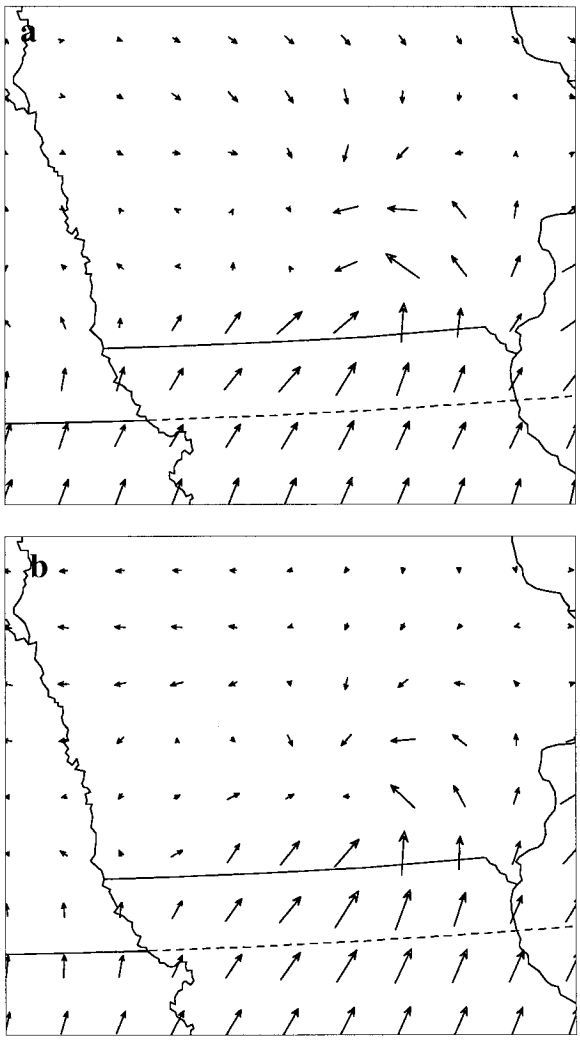

FIG. 2. (a) The storm-relative model winds $\mathbf{V}_m$ and (b) the storm-relative balanced winds $\mathbf{V}_b$ on the 771-mb surface at 23/2200. The maximum wind vector represents a speed of 20 m s^{-1}. Storm motion for this and subsequent figures is $U_s = 7$ m s^{-1}, $\mathbf{V}_s = -5$ m s^{-1}, unless otherwise stated. Note also that in this and later figures with wind vectors, the vectors are plotted *at every other model grid point* in both dimensions.

At later times, the model flow still remains reasonably balanced. Figure 3 shows the wind vectors $\mathbf{V}_b$ and $\mathbf{V}_u$ on the 535-mb surface, when the storm is mature. The slight anticyclonic tendency of the unbalanced winds $\mathbf{V}_u$ (Fig. 3b) is still evident (again note the difference in wind vector scales between panels). The rear-inflow jet shows up well in the northerly component of the balanced winds (Fig. 3a) over Iowa. Here, $\mathbf{V}_u$ also shows a weak (~ 4 m s^{-1}) flow along the Iowa/Illinois border. This unbalanced feature is rather atypical of the unbalanced flow as a whole in that it was composed largely of $\mathbf{V}_{u\Psi}$, the *nondivergent component* of the unbalanced circulation.

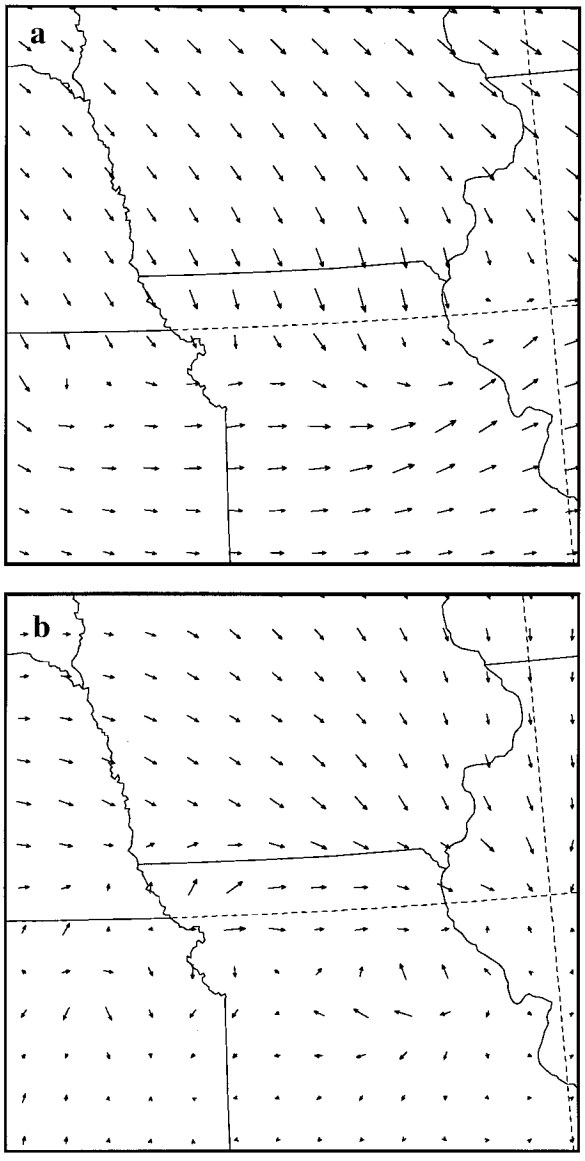

FIG. 3. Both panels at 24/0430 on the 535-mb level. (a) The balanced winds $\mathbf{V}_b$. The maximum wind vector represents a speed of 30 m s^{-1}. (b) The unbalanced winds $\mathbf{V}_u$, maximum speed of 6.7 m s^{-1}.

TABLE 2. The π levels in the analysis domain and their mb equivalents. The fourth column lists, for reference, the associated geometric heights of each surface for a point near the midpoint of the Iowa/Missouri border at 23/1800.

Analysis level	π (J K^{-1} kg^{-1})	Pressure (mb)	Height (m)
1	963.0	864.3	1387.8
2	932.1	771.3	2369.8
3	901.3	685.6	3360.2
4	870.4	607.0	4356.5
5	839.5	535.0	5361.3
6	808.7	469.3	6375.1
7	777.8	409.6	7396.8
8	746.9	355.5	8425.8
9	716.1	306.7	9462.6
10	685.2	262.9	10 514.0
11	654.3	223.8	11 586.4
12	623.5	189.0	12 686.7
13	592.6	158.3	13 828.3
14	561.7	131.3	15 017.8
15	530.9	107.7	16 257.1
16	500.0	87.4	17 555.1

Bulk characteristics

1) VOLUME AVERAGES

To gain an understanding of the atmospheric balance of the storm region as a whole, it is useful to define some bulk measure of the relative significance of the various wind fields by defining an average mass-weighted mean square, or kinetic energy-type measure[1] per unit mass ($\Re$) associated with the various divergent and wind fields:

$$\Re_i = \frac{\int_\Omega (\rho/2)\mathbf{V}_i\cdot\mathbf{V}_i \, d\Omega}{\int_\Omega \rho \, d\Omega}, \tag{12}$$

where Ω represents a volume of integration and $\boldsymbol{\rho}$ the pseudodensity appropriate to the coordinate system. Using the appropriate wind fields in (12), $\Re_{;m}$, $\Re_{;u}$, $\Re_{u\psi}$, and $\Re_{u\chi}$ were computed at half-hour intervals in an averaging volume whose horizontal projection is shown in Fig. 1a.[2] The (pressure) depth of the volume was that of the analysis domain (refer to Table 2 in appendix B). This stationary volume, with a radius of 450 km, was of sufficient horizontal extent to contain most of the vertical motion directly related to the MCC during its lifetime.

Figure 4 shows the time evolution of the various $\Re$s normalized by $\Re_m$, the model kinetic energy. At 23/1900 (-5 h on the ordinate in the figure), the top curve of the main plot in Fig. 4 shows that $\Re_u$ was only about 1% the magnitude of $\Re_m$, again in good agreement with the quasi-balance assumption. With the onset of con-

[1] It should be borne in mind that the only true kinetic energy, in the physical sense, is that associated with the total model horizontal winds, $\mathbf{V}_m$. Due to the quadratic nature of (12), the sum of the unbalanced and balanced $\Re$s, ($\Re_u$,$\Re_b$), does not equal the total $\Re_m$computed from the model winds.

[2] Several volume sizes were tried. Unless stated, the results presented in this section were relatively insensitive to the size of the averaging volume, though of course very large domains showed a smaller amplitude since they included more undisturbed model circulations.

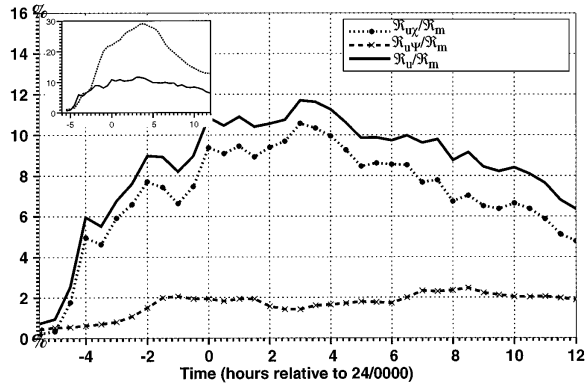

FIG. 4. Here, $\Re$ as defined in Eq. (12) normalized by the volume-average kinetic energy per unit mass, $\Re_m$. The top (solid line) is $\Re_u$ associated with the total unbalanced flow, $\mathbf{V}_u$. The dotted line with filled circles is $\Re_{u\chi}$, associated with the unbalanced divergent flow, $\mathbf{V}_{u\chi}$. The bottom (dashed) line is $\Re_{u\Psi}$, associated with the unbalanced nondivergent flow $\mathbf{V}_{u\Psi}$. The inset plot in the upper-left hand corner displays $\Re$ associated with the residual: $\mathbf{V}_R = \mathbf{V}_m - \mathbf{V}_{b\Psi}$, that is, the difference between the model winds and the balanced nondivergent winds. The top curve in the main figure, $\Re_u/\Re_m$, is plotted in the inset (bottom curve) for comparison. Note the scale difference on the abcissae. Refer to Fig. 1a for the location of the averaging volume.

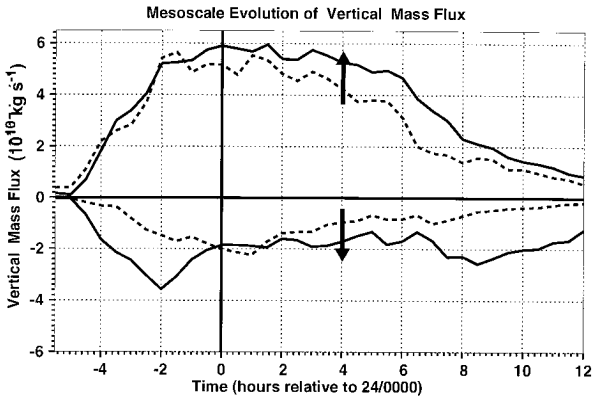

FIG. 5. Area-integrated upward and downward vertical mass flux (10^{10} kg s^{-1}) through the 535-mb surface. The solid lines indicate the fluxes by ω_m and dotted lines, mass fluxes by ω_b. The time axis is the same as in Fig. 4. The averaging area is indicated in Fig. 1a.

vection, the ratio $\Re_u/\Re_m$ quickly grew to several percent. At the time of maximum extent of the storm, between 24/0200 and 24/0400, $\Re_u/\Re_m$ reached almost 12%. As the storm dissipated, the ratio slowly fell, decreasingly more or less linearly after 24/0730, when the convection had ceased. By the end of the simulation (24/1200), $\Re_u/\Re_m$ was still over 6%, several times larger than the pre-convective value at 23/1900.

The dotted (middle) curve in Fig. 4, with the filled-circle symbols, shows the evolution of $\Re_{u\chi}$ associated with $\mathbf{V}_{u\chi}$, while the dashed (bottom) curve shows $\Re_{u\Psi}$, associated with the $\mathbf{V}_{u\psi}$. Throughout the time series, $\Re_{u\chi}/\Re_m$ closely tracks $\Re_u/\Re_m$, both in amplitude and trend. In comparison, $\Re_{u\Psi}/\Re_m$ does increase, but only gradually, exceeding 2% for just a short period (24/0600 $\rightarrow$ 24/1000) near the end of the storm.

The unbalanced $\Re$ evolution shows several interesting features about the bulk flow behavior of the storm, the most obvious (and anticipated) result being that the total unbalanced flow is largely divergent. A significant pulsing is apparent as a ripple superimposed on the general trend of $\Re_u/\Re_m$. Even in the earliest stages of the storm development, this pulsing is apparent. This is not present in $\Re_{u\Psi}/\Re_m$ and it is speculated that this higher frequency oscillatory behavior is likely associated with gravity wave motions (see related discussion in section 4c). A similar pulsing was found in the two-dimensional MCC modeling studies of Tripoli and Cotton (1989).

The inset in the upper-left hand corner of Fig. 4 shows the $\Re$ associated with the quantity $\mathbf{V}_m - \mathbf{V}_{b\Psi}$, the difference between the model winds and the balanced nondivergent winds. This quantity has a maximum approaching 30%. Obviously the balanced divergent flow $\mathbf{V}_{b\chi}$, is, at least locally, an important component of the total balanced winds. (Recall that $\Re_u$ is calculated using the residual $\mathbf{V}_m - \mathbf{V}_{b\Psi} - \mathbf{V}_{b\chi}$. This is the top curve in the main figure and also appears for reference in the inset figure as the lower curve.) Some balanced models (e.g., Raymond and Jiang 1990) neglect advection by $\mathbf{V}_{b\chi}$, the balanced divergent wind. Any balanced model that neglects advection by $\mathbf{V}_{b\chi}$ would be expected to exhibit significant errors in regions of strong convection.

2) AREA-INTEGRATED VERTICAL FLUXES IN THE MIDTROPOSPHERE

The area-integrated vertical mass flux through the midtroposphere provides a good bulk measure of the consistency between the model-produced vertical motion, ω_m, and the balanced vertical motion, ω_b. Figure 5 shows the area-integrated upward and downward mass flux through the 535-mb surface as a function of time.

What is most apparent in this figure is that the upward flux from both ω_m and ω_b exceeds the downward flux during almost the entire lifetime of the storm.[3] The positive vertical mass fluxes, $\phi_{m+} = \Sigma\rho\omega_{m+}$, $\phi_{b+} = \Sigma\rho\omega_{b+}$, are almost identical during the first 3 h of convection. After 23/2300, ϕ_{m+} exceeds ϕ_{b+} for the duration of the simulation with the largest values of both ϕ_{m+} and ϕ_{b+} occurring between 24/0000 and 24/0130, and then de-

[3] As the storm matured, a large anvil cloud developed to the north and east of the convective line as a result of the considerable westerly shear above 6000 m. The evaporative cooling of over -10 C h^{-1} below this anvil cloud forced mesoscale downdrafts. Due to the eastward dislocation of these downdrafts relative to the convective updrafts, an increasingly large amount of diabatically forced downward motion occurred outside the averaging domain after 24/0700. Before this time, almost all the vertical motion directly induced by *diabatic* processes occurred within the domain. This effect can be seen in the decreasing magnitude of ϕ_{b-} in Fig. 6 after 24/0700.

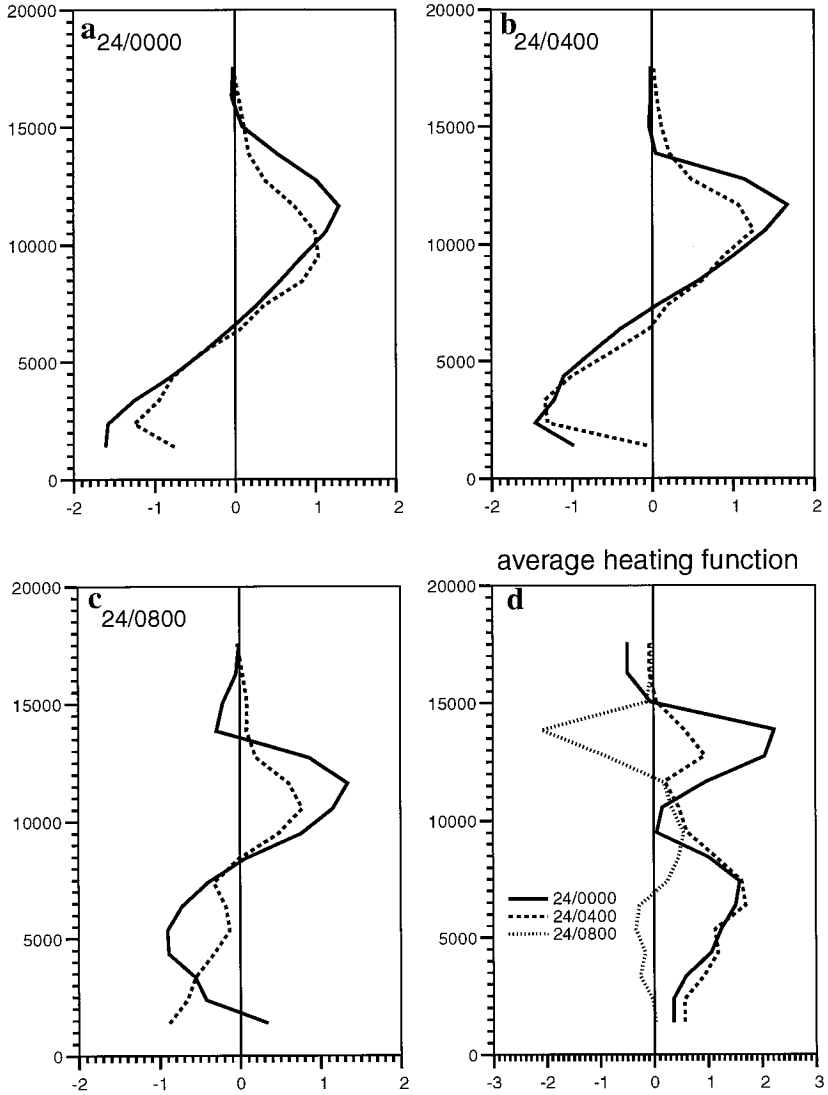

FIG. 6. Two-hour average horizontal mass flux divergence profiles (10^{-5} kg m^{-3} s^{-1}) at (a) 24/0000, (b) 24/0400, and (c) 24/0800. In each of the figures the solid line is the mass flux divergence from the model, while the dashed line is the balanced mass flux divergence. The vertical axis is meters AGL. (d) The area-averaged heating function, Q(z) (°C h^{-1}), for the same three times as the divergence profiles.

creasing only gradually until around 24/0600, as the convective line weakens.

It is interesting to note that the residual *unbalanced* upward mass flux,

$$\phi_{u+} = \phi_{m+} - \phi_{b+},$$

increases from 24/0100 onward until 24/0700, well into the dissipating stage of the MCC. During this time, the stratiform region of the storm is enlarging. Concurrently, below the stratiform region, the rear inflow is developing as precipitation evaporates into the dry midlevel air. This broad region of cooling modifies the mean vertical profile of the heating function, *Q(z)*. A change in heating function, $dQ(z)/dt$, has been shown to produce gravity waves (Emanuel 1983; Mapes 1993, hereafter M93). The increase in both ϕ_{u+} and the unbalanced downward flux, ϕ_{u-}, correlates well with the development of a much more complex *Q(z)* (Fig. 6d). By 24/0800, *Q(z)* is dominated by evaporative cooling and ϕ_{u+} slowly decreases as the waves propagate out of the averaging domain.

The downward mass fluxes in Fig. 5, ϕ_{m-} and ϕ_{b-}, show considerably less consistency than their positive counterparts. The downward model mass flux, ϕ_{m-}, rapidly increases from the time of the first convection until 23/2200, corresponding to the brief period when

$\phi_{b+} > \phi_{m+}$. After this time, ϕ_{m-} dramatically weakens, remaining more or less constant through the rest of the storm lifetime. By contrast, ϕ_{b-} gradually increases in magnitude from the time of first convection until 24/0130 and then slowly returns to near zero by the end of the simulation. The time evolution of ϕ_{b-} generally resembles a smaller amplitude, inverse image of its positive counterpart ϕ_{b+}.

3) AVERAGED DIVERGENCE PROFILES

Before leaving the discussion of the divergent flow, it is instructive to consider some vertical profiles of the average horizontal mass flux divergence,

$$\bar{D}(z) = \frac{\int \nabla\cdot\rho\mathbf{V}_i \, dA}{\int dA} \qquad i = m, b \tag{13}$$

for each of the levels in the averaging volume. Figure 6 shows such 2-h time-average profiles centered at 24/0000, 24/0400, and 24/0800. The solid line in each panel is the model mass-flux divergence, $\overline{D}_m$, and the dashed line, $\overline{D}_b$, the mass-flux divergence associated with the balanced wind.

The first two times (24/0000 and 24/0400) reveal several of the same features. As expected, both $\overline{D}_m$ and $\overline{D}_b$ show convergence at lower levels, with divergence in the upper half of the troposphere. The level of maximum convergence (~2500 m) is the same for both $\overline{D}_m$ and $\overline{D}_b$. Here, $\overline{D}_b$ consistently shows a level of maximum divergence somewhat lower and weaker than $\overline{D}_m$; $\overline{D}_b$ also shows weaker convergence at the lowest level throughout the convective portion of the storm. In general, however, the balanced divergence and model divergence profiles at 24/0000 and 24/0400 are in good agreement and show strong similarities to observed MCS divergence profiles (e.g., Fig. 2 of M93 and Fig. 12 of Cotton et al. 1989).

At 24/0800 (Fig. 6c), $\overline{D}_m$ and $\overline{D}_b$ show much poorer agreement. By this time, the latent heating has largely ceased, with the exception of two confined regions near the decadent squall line. The average heating function, $\overline{Q(z)} = \overline{d\theta\/dt}$ (Fig. 6d) computed from the numerical simulation has changed significantly from 24/0400 to 24/0800. The level of maximum convergence for the model flow has moved upward to 5000 m from 2500 m earlier. Here, $\overline{D}_m$ is now positive (divergent) at the lowest level, while $\overline{D}_b$ shows its strongest convergence there. The model surface wind fields (below the bottom of the balanced-analysis domain) have a strong flow of relatively cool air away from the storm.

Throughout the evolution of the simulated MCC, $\mathbf{V}_b$ showed a systematic tendency to have a lower level of maximum divergence relative to $\mathbf{V}_m$. While the divergence profiles show a very pronounced maximum in $\overline{D}_m$, which remains at a height of about 11 500 m, $\overline{D}_b$ shows a less pronounced maximum at about 10 000 m. In the PE model, the detrainment from the updrafts occurred over a very thin level, just at the tropopause, creating the sharply peaked maximum of $\overline{D}_m$.

4. Discussion

Historically, balance approximations were referred to as filtering approximations, as they ''filtered'' out behavior (e.g., gravity waves, acoustic waves, Lamb waves) deemed undesirable in a numerical model (Haltiner and Williams 1980; Holton 1992). The neglect (filtering) of gravity wave oscillations by balanced models is equivalent to the assumption that the gravity wave phase speed (c)$\rightarrow \infty$, that is, that gravity waves radiate away immediately. This does not mean that the *effects* of gravity wave propagation in a rotating fluid are not contained within the theory, but rather that the transient adjustment process happens *instantaneously*, resulting in only the slow-manifold, balanced flow. The scale over which these adjustments occur is given by the Rossby radius (or ''radius of deformation''), λ_R. The difference between the balanced and model circulations in the present application largely represents transient or fast manifold processes, typically of an oscillatory nature, which have no representation in the balance paradigm. Some of those processes are considered here.

a. Compensating subsidence

The differing nature of the upward and downward midtropospheric fluxes discussed in section 3 suggests that the model dynamics forcing upward motion within the averaging domain are different from those that drive the downward motion. The relatively close agreement between ϕ_{m+} and ϕ_{b+} indicates that the main driving process for *updraft* motion, latent heat release resulting from cloud microphysical processes, is instantaneously well-represented in the NLB ω-equation solution. By contrast, the inconsistency between ϕ_{m-} and ϕ_{b-} indicates that the dynamics driving *downward* motion within the averaging domain are relatively poorly represented in that solution. The location of the balanced downdrafts causing the modest ϕ_{b-} seen in Fig. 5 correlate well with the evaporative cooling behind, and to the east, of the convective line. The quite different behavior of ϕ_{m-} indicates that the PE model is responding to more than the direct evaporative cooling felt by the balanced ω equation.

The difference between ϕ_{m+} and ϕ_{m-} graphically illustrates a well-known and important aspect of so-called compensating subsidence (i.e., that downward motion necessary to maintain continuity in a large-scale integrated sense)—the mass flux locally forced in buoyantly driven updrafts results in downward motion on a much greater scale. The difference between ϕ_{m-} and ϕ_{b-} highlights another point: *The mechanisms by which compensating subsidence occur are largely fast manifold processes not contained in balanced model theories, which exclude inertia-gravity and acoustic wave motion.*

The nature of compensating subsidence has received recent attention in several studies (e.g., Bretherton and Smolarkiewicz 1989; Nicholls et al. 1991; Schmidt and Cotton 1990; M93). Results of Bretherton and Smolarkiewicz (1989) and Nicholls et al. (1991), for a nonrotating atmosphere at rest, have shown that the disturbances forced by the initiation or termination of an imposed heating function (i.e., a nonzero dQ/dt as discussed above) have the propagation mode associated with gravity waves. Therefore, results from gravity wave theory are applicable. The predicted horizontal gravity wave propagation speed for a wave with vertical wavenumber m,

$$c_x = N/m = NH/n\pi, \tag{14}$$

is indeed found by Nicholls et al. In (14), H is a scale height, n a positive integer, and N the Brunt–Väisälä frequency.

Unlike classical linearly superimposed gravity waves, such propagating ''buoyancy bores'' *do not* have a spatial or temporal periodicity and *do* leave a permanent net horizontal displacement in the fluid through which they propagate (M93). These bores then must transport (rearrange) mass in a stratified fluid, and evidently represent the agents of compensating subsidence, enabling the fluid to recover a state of mass equilibrium. Because of their gravity-wave-like nature, such bores would not be explicitly represented in balanced models, yet the volume integral of (6), the continuity equation, still must be satisfied, and the compensating subsidence must almost immediately occur in a more global sense, being spread over a much larger domain. The midtropospheric ω_b does show evidence of weak subsidence across a very large region of analysis domain (much larger than the averaging volume) over which the stronger directly diabatically induced vertical motions are superimposed.

In an infinite, inviscid, nonrotating domain, the buoyancy bore would radiate to infinity, leaving no trace of itself in the winds or temperature structure of the fluid. Gravity waves in a rotating fluid, however, become modified (deformed) as they propagate away from their source, with λ_R being the length scale over which this occurs. The irreversible, horizontal displacement of the fluid caused by the passage of the bore implies a vertically varying horizontal motion that in turn, requires a balancing horizontal temperature gradient (Gill 1982). The buoyancy required by the balancing horizontal thermal structure comes from the bore itself. Hence, the bore becomes, in a sense, absorbed, as it propagates outward, leaving energy behind in the balancing or adjustment process. The rotational dynamics that scale with λ_R are contained in the NLB equation set. This suggests a length scale or ''e-folding'' length governing the balanced compensating subsidence in the balanced ω equation.

In the idealized approach of M93 the passage of the buoyancy bore caused ''area contraction,'' that is, a large-scale low-level convergence. To the extent that the balance approximation is valid, the balanced wind and mass fields at any give time could be expected to represent the final adjusted state (which may or may not include such an area contraction) after all transients, such as buoyancy bores, have passed. However, since the transient motions are not represented in the NLB model, any meteorological phenomena that inherently depend on, or are triggered by, the transient motions themselves would not be captured in a balanced model simulation. Studies in the literature have found the oscillatory nature of gravity waves to mediate several phenomena such as squall line propagation (e.g., Cram et al. 1992) and convective initiation (e.g., Crook 1987; Zhang and Fritsch 1988b; Crook et al. 1990; Schmidt and Cotton 1990). A balanced model, by filtering out fast-manifold oscillatory motion, will have several potential limitations when simulating phenomena that rely on rapid vertical parcel displacements.

b. Some further aspects of the unbalanced flow

Potential vorticity is a conserved property in the inversion process in the sense that the resulting balanced wind and thermal structure yield the same PV produced by the model. This does not, however, mean that the same wind and thermal fields are recovered. Rather, the agreement depends on how well the balance assumption is met. (The filtering of negative PV also causes a minor difference, because the model fields, $\mathbf{V}_m$ and θ_m no longer agree with the positive-definite PV field used in the inversion.) Figure 7a (23/2200) shows the midtropospheric wind vectors and relative vorticity (ζ_m), while Fig. 7b shows the nondivergent component of the unbalanced winds, $\mathbf{V}_{u\Psi}$, and the associated unbalanced vorticity,

$$\zeta_u = \zeta_m - \zeta_b, \tag{15}$$

found by taking $\nabla\times$ (10). The $\mathbf{V}_{u\Psi}$ field shows a definite anticyclonic flow, in agreement with ζ_u in Fig. 7b, implying that $\mathbf{V}_b$ is more cyclonic than $\mathbf{V}_m$. For PV to be maintained, this would then necessitate that the balanced θ field is less stable than the model θ field. Figure 7c shows the difference Brunt–Väisälä frequency,

$$N_u = N_m - N_b. \tag{16}$$

.

As expected, $N_u > 0$ over most of this region, which implies $N_b < N_m$, that is, the balanced θ field is less stable than the model fields.

This difference between the model and balanced fields must result from a number of factors besides the filtering process since, at this early time in the storm evolution, only a very small region of weak negative PV is found. The NLB approximation to PV assumes that $\partial\mathbf{V}_\chi/\partial z \ll \partial\mathbf{V}_\psi/\partial z$, which is typically a poor assumption within, and ahead of, the convective line (e.g., Skamarock et al. 1994). The hydrostatic assumption is also included in the NLB PV approximation, eliminating horizontal

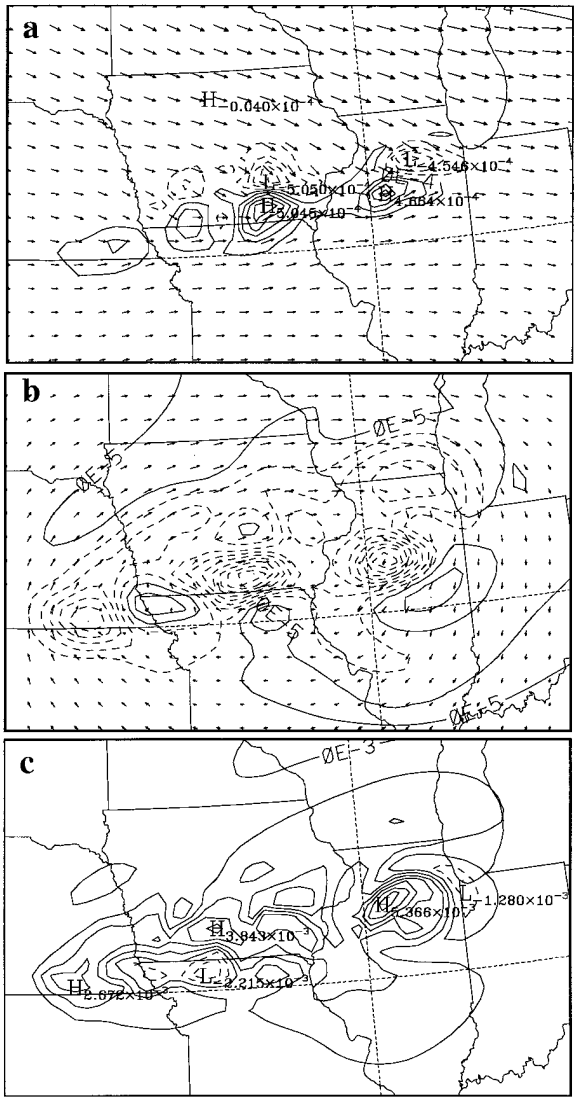

FIG. 7. All plots at 23/2200 on the 535-mb surface. (a) The model winds, $\mathbf{V}_m$, and relative vorticity ζ_m. The maximum wind vector represents a speed of 27 m s^{-1}. The contour interval for the vorticity is 1×10^{-4} s^{-1}. (b) The unbalanced nondivergent winds, $\mathbf{V}_{u\Psi}$, and the associated unbalanced vorticity ζ_u. Here, the maximum wind speed is 2.2 m s^{-1}, and the contour interval is 0.5×10^{-5} s^{-1}. (c) The difference Brunt–Väisälä frequency N_u as defined by (16), contour interval of 8×10^{-4} s^{-1}.

shear of the vertical winds ($\partial\omega/\partial x$, $\partial\omega/\partial y$). With vertical velocities in the convective updrafts of a few meters per second in close proximity to downdrafts of similar strength, this can also be a poor approximation near the squall line. There is a high spatial correlation between the extrema in ζ_u, N_u, and ω (not shown) at this level, that is, these extrema are located in the region near the updraft and downdraft cores, where the motion is likely nonhydrostatic. The difference between ζ_m and ζ_b locally exceeds 10%. This difference decreases rapidly with distance to the south but less rapidly to the north. The flow accelerating into the storm from the north has a strong divergent component that increases with height in the lower- and midtroposphere. Again, this contribution to PV is neglected in the NLB approximation. Still, even in light of the differences discussed above, the rapidly developing storm system is balanced to a remarkable degree.

c. Use of NLB diagnostics as a gravity wave filter

As mentioned earlier the unbalanced flow represents the fast manifold residual of the balanced filtering process. Before the divergent motions become complicated by interfering waves of differing wavelengths, the filtering capacity in this application is quite evident, even in the unbalanced horizontal winds.

A clear example of this is seen in Fig. 8 (23/2200) which shows ω_u on the 607-mb surface. The contouring has been limited to the range -0.5×10^{-3} to 5×10^{-3} m^2 s^{-3} K^{-1} to emphasize the periodic motion. At this time, the mesoscale ω_u is the combination of two superimposed nearly radially symmetric wave patterns. The western source has not been in existence as long and as a result the first outgoing wave has not propagated out as far as the eastern pattern. The eastern pattern is the eastward-advecting remnant of the first short-lived convective pulse (Part I), which fired over central Iowa shortly before 23/2000.

The filtering ability of the balanced analysis is useful in comparing some aspects of the unbalanced flow behavior to that predicted by gravity wave theory. An example is the problem of convective mass adjustment or compensating subsidence touched upon in section 4a. M93 proposed that a heating profile typical of tropical MCSs,

$$Q(z) = Q_0[\sin(\pi z/H) + \sin(2\pi z/H)/2], \quad (17)$$

would produce a divergence profile of the form

$$D(Q, z) = \frac{-\pi\rho Q_0}{HN^2}[\cos(\pi z/H) - \cos(2\pi z/H)/2]. \quad (18)$$

In (17) and (18) $\pi \approx 3.14159$, N is the Brunt–Väisälä frequency, and H is the depth of the domain. A sketch of $Q(z)$ and $D(z)$ appear to the far left in Fig. 9. The shape of the idealized divergence, $D(z)$, agrees quite well with the lower two-thirds of the ''early-MCC'' divergence profile in Fig. 6a.

Instantaneously imposing Q in a stratified atmosphere should result in a gravity wave motion corresponding to two lowest-order vertical modes. The gravest mode, of vertical wavenumber 1/2 (M93's $l=1$ bore), resulting from the first term in (17) would be a half sine wave of negative vertical motion, $-w_0\sin(\pi z/H)$, while the second mode, with vertical wavenumber 1 would consist of an up-and-down couplet.

Using the equations developed by Bretherton and Smolarkiewicz (1989), M93 calculated the displacement of a surface, $\Delta z(r,t)$, for the radially symmetric case.

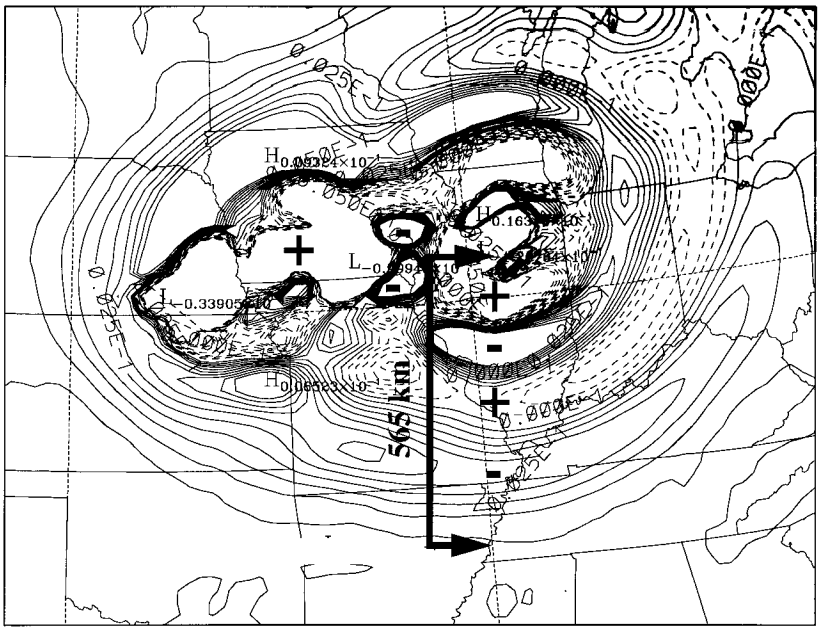

FIG. 8. The unbalanced vertical velocity ($\omega_b = d\pi/dt$) at 23/2200 on the 607-mb surface. The contour level is 5×10^{-4} m^2 s^{-3} K^{-1}. The contouring has been limited to the range $-5 \times 10^{-3} \rightarrow 5 \times 10^{-3}$ to emphasize the wavelike vertical motion at distances well removed from the convective region. The "+" and "−" signs denote regions of upward and downward motion, respectively. (In the π vertical coordinate, positive values imply negative vertical motion). The bold double ended arrow indicates the approximate distance the leading wavefront has propagated in the 3-h period since convection began.

After a propagation time τ, the bores have traveled L and $2L$, where $L = c_2\tau$, c_2 being the propagation speed of the higher-order bore. Using $N = 10^{-2}$ s^{-1} and $c = 50$ m s^{-1}, M93 found $2L$ to be about 550 km (see his Fig 4).

The clear gravity wave pattern in Fig. 8 permits an application of this theory to the PE simulation. From the center of the pattern southward, the leading edge of the storm-induced vertical motion is about 565 km. The convection has been active for about 3 h, giving a propagation speed of 51 m s^{-1}. The Brunt–Väisälä frequency on the 607-mb surface south of the storm region at 23/2200 is an almost constant 1.42×10^{-2} s^{-1}. The propagation speed of a linear gravity wave is given by (14). Using these values in (14), the inverse of the vertical wavenumber is $m^{-1} = 3584$ m, giving a value for H of 11.3 km. From Fig. 4a in Part I, the tropopause height in the southern end of the cross section can be estimated from the PV gradient as about 11 km, which agrees very well with the computation of H above. The vertical motion depicted in Fig. 9 closely matches that along the heavy line in Fig. 8, with subsidence from about 300 km south to 565 km south, and a rapid shift to positive vertical motion at about the 300-km point. A plot similar to Fig. 8 on the 356-mb surface (not shown) shows a broad subsidence in qualitative agreement with Fig. 9, though at this level the radial pattern evident at 607 mb is quite distorted by the strongly sheared flow.

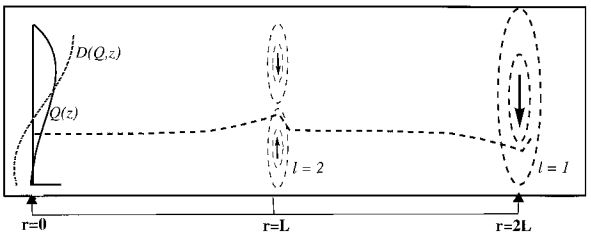

FIG. 9. Schematic depiction of the results of M93. The line plot above r=0 shows the heating function Q(z) (solid). The dotted line in the line plot shows the resulting divergence profile D(Q,z) expected in the region $0 < r < L$. After a propagation time τ, the l=2 and l=1 bores have traveled L and $2L$, respectively. The horizontal dashed line indicates the relative displacement of a surface in the lower half of the domain. Adapted from Fig. 3 of M93.

The more detailed wave structure closer to the storm is due to higher wavenumber oscillations with slower propagation speeds. Using (14) with n=2 gives a horizontal phase speed of 25.5 m s^{-1} for the second mode, with a corresponding wavelength of about 280 km, as compared to 25.0 m s^{-1} and 250 km, respectively, for n=2 in M93. These values are similar to those in Zhang and Fritsch (1988b), where internal waves associated with a simulated MCS had 25–30 m s^{-1} phase speeds and wavelengths of 250–300 km. Considering that the work of M93 was highly idealized, with horizontally

homogeneous initial conditions and no shear, topography, or Coriolis force, the close agreement with this PE simulation of an MCC is notable.

d. The Rossby radius revisited

In an attempt to define a metric that determines the dynamic size (and implicitly, the relative state of balance) of an MCC, Cotton et al. (1989) proposed a dynamic definition for MCCs:

> A mature MCC represents an inertially stable mesoscale convective system that is nearly geostrophically balanced and whose horizontal scale is comparable to or greater than λ_R.

From the discussion of balance approximations in section 2 it should be apparent that the use of the term ''geostrophic'' by Cotton et al. in this definition is too restrictive. Geostrophic balance implies that (at the level of the *f*-plane approximation) the nonlinear term in square brackets in (2) is zero, a manifestly poor approximation in the application to MCCs. With the restriction to geostrophy relaxed, however, the above definition still provides a useful dynamic metric.

Cotton et al. (1989) used a form of the Rossby radius (Schubert and Hack 1982; Frank 1983) that accounts for locally enhanced vorticity:

$$\lambda_R = \frac{c_n}{(\zeta + f)^{1/2}(2VR^{-1} + f)^{1/2}}, \tag{19}$$

where ζ is the relative vorticity, V the tangential velocity at some radius R, f the Coriolis parameter, and c_n the phase speed of the nth mode pure gravity wave. The quantity in the denominator of (19) is the square root of the inertial stability parameter (Schubert and Hack 1982). The form of λ_R in (19) reduces to the more familiar result (Gill 1982)

$$\lambda_R = c_n/f, \tag{20}$$

in the absence of significant relative vorticity and curvature, that is, as $\zeta \to 0$ and $R \to \infty$. This form has the clear interpretation as the distance a wave would travel during the rotational timescale $1/f$.

MCSs typically develop a strong positive vorticity maximum (and associated PV anomaly) in the lower and middle troposphere (e.g., Schubert and Hack 1982; Raymond and Jiang 1990; Hertenstein and Schubert 1991; Fritsch et al. 1994; Hertenstein 1996; Part I). Cotton et al. (1989) argue that as an MCC develops this maximum, it achieves greater inertial stability, and, hence, a smaller λ_R. The inertial stability (the horizontal analog of static stability) provides a measure of the horizontal restoring force resisting lateral displacements. Enhancement of the inertial stability is often referred to as ''stiffening'' (Ooyama 1982; Schubert and Hack 1982). For systems smaller than λ_R, the energy (here in the form of CAPE) released in the deep convection excites gravity waves, which effectively radiate energy from the system. For MCSs larger than λ_R, more of the released energy is confined locally to within the storm, and is projected into the rotational flow. In support of their dynamical definition, Cotton et al. (1989) cite observational studies (e.g., McAnelly and Cotton 1986, 1989) showing that as an MCC matures, the system becomes less divergent and the vertical motion less pronounced, in agreement with the reasoning of Ooyama (1982) that the balanced dynamically large system is more characteristically two-dimensional.

This argument is supported by the findings of Schubert et al. (1980). Using a linearized axisymmetric vortex model, they found that convective-type heating in a basic state with no relative vorticity produced a response dominated by inertia–gravity waves, with very little energy going into the rotational spectrum of modes. When the basic state was one in which the inner region had positive relative vorticity, and hence a greater inertial stability, the heating became much more efficient in producing a balanced vortical flow. In the former case, energy was radiated away, whereas in the latter case the energy was largely confined to the storm-scale circulations. Hack and Schubert (1986), using an axisymmetric PE model, further quantified this argument by demonstrating that the nonlinear effects of diabatic heating on acceleration of the tangential winds depend significantly on the immediate state of the large-scale circulation.

Zhang and Fritsch (1988a) suggest that the convective moistening of the atmosphere in a region of positive relative vorticity produces a further stabilizing influence through what they term the ''virtual temperature effect.'' They argue that a 1°C increase in T_v through the virtual effect could account for a significant portion of the geopotential perturbation observed in long-lived midlatitude vortices and that this may be especially important in the genesis stage of MCVs since, unlike sensible heating, the local effects of moistening (virtual warming) cannot be dissipated by gravity–inertia waves.

The work of DW offers a contrasting viewpoint of the importance of large-scale inertial stability to vortex formation and longevity. The numerical simulations of Skamarock et al. 1994 and DW demonstrated that balanced squall line ''end vortices'' can form even in the absence of background absolute vorticity. DW suggest that the significance of inertial stability depends on scale, and that for scales less than 100 km, existence of weak low-level shear is a more dominant factor.

Clearly, the viewpoint of DW not withstanding, inertial stability provides a tremendously important constraint on the motions excited in the atmosphere as a response to thermal forcing. Unfortunately, the previous theoretical studies have used idealized geometries (i.e., axisymmetry) and other approximations and simplifications such as ideal vortex structure and linearization that may lead to analytic solutions, but whose applicability to the fully three-dimensional MCC is not well defined. Many, if not most, MCCs have a linear structure in the leading edge of the convection. Regrettably, no

fully three-dimensional theory of inertial stability exists for the general case.

To apply (19) to their composite MCC, Cotton et al. (1989) chose R to be ~320 km, corresponding to the radius of the cloud shield with temperature ≤ -33°C. A problem arises in calculating the appropriate gravity-inertia phase speed from (14) to use in these calculations of λ_R, since the Brunt–Väisälä frequency shows considerable temporal and spatial variation. Further, there are different phase speeds (and hence a distinct λ_R) for each vertical mode. Phase speeds can vary from $\sim 3 \rightarrow$ 300 m s^{-1} (Schubert et al. 1980), giving a wide range of values for the different λ_R. Cotton et al. chose a value of 30 m s^{-1} based on results of a two-dimensional simulation by Tripoli and Cotton (1989). Using these values at a latitude of 40°, they computed $\lambda_R = 300$ km for the composite MCC. This λ_R was slightly smaller than their cloud shield radius R, of about 320 km. Other researchers have found similar values for the Rossby radius (e.g., Johnson and Bartels 1992).

While the interpretation of λ_R is fairly clear for simple systems, caution needs to be exercised in interpreting the calculated values for λ_R in Cotton et al. (1989) and in the present context since both the static stability and vorticity generally show considerable variation within the domain. The approach used here is to define ''typical'' values of the necessary variables in the appropriate context, and other choices can arguably be equally valid. It should also be borne in mind that a different λ_R exists for each mode of vertical wave structure. The resultant $\lambda_R(m)$ may be considered a scale or ''*e*-folding'' length appropriate *to that mode*. Some adjustment still occurs for distances greater than λ_R.

The analysis of the unbalanced flow presented earlier offers some specific guidance in the computation of λ_R in our study. While several factors can locally influence the value of c_n, the calculations of λ_R discussed below assume that c_n as calculated for the large-scale environment is appropriate. The suitability of this choice is discussed in appendix C. Using the more conventional notation for λ_R in (20) (a deformation radius appropriate to the large-scale storm environment) and the phase speeds found earlier, yields values of 509 km and 255 km for the first 2 modes, respectively. Where the vorticity is significantly perturbed by the MCC, λ_R as computed using (19) will be smaller. The PE simulation discussed in Part I indicates that an MCC has several important structures, each having a relevant length scale. The vorticity can also vary by several hundred percent, even in somewhat radially shaped features. Still, (19) may be applied, at least heuristically, with some guidance from the balanced analysis.

Several of the features within the MCC are clearly balanced. For example, the MCV, which formed early in the storm, has $R \approx 100$ km, and $\zeta \approx 3.5 \times 10^{-4}$ s^{-1} as an average over the storm-relative closed circulation. Using $f = 1.0 \times 10^{-4}$ s^{-1} and $V \approx 10$ m s^{-1}, $\lambda_R = 138$ km for the n $=1$ mode and $\lambda_R = 69$ km for the second mode. This result is not surprising, in light of the good agreement between $\mathbf{V}_m$ and $\mathbf{V}_b$ in the vortical circulation in Fig. 2. Typical values for the mature storm as a whole might be $R \approx 250$ km, $\zeta \approx 1.5 \times 10^{-4}$ s^{-1}, $f = 1.0 \times 10^{-4}$ s^{-1}, $V \approx 15$ m s^{-1}. Assuming the phase speeds above are appropriate, $\lambda_R = 214$ km for the gravest mode and $\lambda_R = 107$ km for the second vertical mode.

The circulations attributable to the MCC certainly exceed 200 km in scale. This analysis also suggests that all higher order vertical modes would be strongly modified before they could propagate a great distance from the storm, while the first mode would radiate a significant amount of energy away from the MCC. These λ_R calculations, while imprecise, further support the conclusion that the MCC in this study is, to a large extent, a balanced system.

5. Summary and conclusions

This and a companion paper (Part I) are an attempt to resolve the question: *Does the MCC represent a balanced fluid-dynamical system?* The answer to that question is, to a large extent, *yes*, at least for this simulated case. The nondivergent component of the PE model winds was found to consist, to a great degree, of balanced flow, $\mathbf{V}_{b\Psi}$. Further, this was not a state that was achieved after some period of adjustment. Rather, the nondivergent winds, throughout the MCC lifetime, from initial convection to dissipation, remained in a nearly balanced state. This almost ''instantaneous adjustment'' was also observed by DW in their balanced diagnosis of an idealized squall line and associated MCV. Perhaps more surprisingly, the storm-induced divergent model winds also remained balanced to a fair degree, though certainly less so than the nondivergent flow. Further, the *balanced* divergent flow comprises a significant portion of the total balanced flow in some regions of the MCC.

Gravity waves, induced by the intense heating, consist almost entirely of divergent flow, which is unbalanced. The good agreement between model and balanced upward vertical mass flux, together with the periodic wave-like appearance of ω_u and $\mathbf{V}_{u\chi}$ and the known filtering characteristics of the balance model, suggests that the bulk of the three-dimensional unbalanced divergent motion may be attributed to gravity waves.

Within the averaging volume, the greatest disparity between the model and balanced circulations was found in the downward vertical motion. Both ϕ_{b-} and ϕ_{m-}, the integrated downward mass fluxes, were considerably smaller than their upward counterparts, indicating that the subsidence compensating both ϕ_{b+} and ϕ_{m+} occurred over an area much greater than the averaging volume. The model downward mass flux exceeded the balanced downward flux by a factor of 2 at almost all times during the lifetime of the simulated MCC. This suggests that the process of mass adjustment due to convective heating is largely dominated by unbalanced fast-manifold processes, such as inertia–gravity waves, a theory sup-

ported by recent research on the convective adjustment process. This adjustment process, which occurs on a scale much larger than the more confined upward flux, has a much larger timescale and the instantaneous adjustment assumed in the balanced system is evidently less valid for this process.

The ω_u and divergence fields showed strong evidence of the predicted domination by vertical waves 1 and 2. The (modified) Rossby radii for these two lowest-order modes were calculated and it was shown that the MCV within the storm was larger than λ_R for all waves with $n > 1$. The λ_R for the mature storm as an ensemble also predicted a good degree of balance with $\lambda_R{}^{n=1}$ scaling similarly to the MCC. Based on the results presented here, we suggest the following refinement of the dynamic definition for MCCs put forth by Cotton et al. (1989):

> A *mature* MCC represents an *inertially stable* mesoscale convective system that is in a *nearly balanced dynamical state* and whose horizontal scale is comparable to or greater than a locally defined λ_R.

A question related to the representativeness of the MCC as a balanced system is the question: *Can a prognostic balanced model faithfully represent the full evolution of an MCC*? The results presented here and in Part I, when contrasted with those of DW, suggest that the answer might significantly depend on the large-scale environment and initial conditions of the simulation. In the case considered by DW, the storm generation of horizontal vorticity by the divergent cold pool, $d\mathbf{V}_\chi/dz$, a term neglected in the NLB approximation, was essential in the development of the vortical structure seen in their simulation. As discussed in Part I, the MCV in the PE simulation analyzed here did not result from the same mechanism as in DW. Instead this MCV formed by convergence/stretching of ambient vertical vorticity—a mechanism well-represented within the approximations inherent in the NLB system—and as such should be more realizable in a prognostic NLB model. Any definitive resolution to this question, however, will require the application of prognostic balanced models to MCS simulations in a variety of realistic environments. For any situation in which the subsequent evolution of the fluid state depends largely on the mechanics of the transient adjustment process, however, (e.g., the lifting of a parcel beyond its level of free convection by gravity wave oscillations) a balanced model would *not* be expected to perform well.

The results found in this study present a picture of the ''signature'' an MCC leaves in its environment after the decay of transients. Hopefully, this information will be found useful in parameterizing the effects of MCCs and MCSs in general circulation and climate models where such features are typically on the order of a single grid cell. It is often tempting to overgeneralize the results of a particular case study. To determine the applicability of the results presented above to MCCs in general, and other MCSs, it would be useful to apply the balanced analysis used in this paper to other MCC simulations. In particular, it would be illuminating to analyze storms developing in differing environments and at different latitudes.

Acknowledgments. The authors are grateful for the thoughtful advice and encouragement offered from several parties, in particular Rolf Hertenstein, Ute Olsson, Scott Rafkin, and Dr. Robert Walko. Special thanks go to Drs. Wayne Schubert and Michael Montgomery, who were instrumental in the development and understanding of many of the balanced dynamical concepts used herein. Appreciation is also extended to Drs. Hongli Jiang and J. M. Fritsch and to Ray McAnelly and two anonymous reviewers for their careful and constructive reviews of this manuscript. This work was supported by the National Science Foundation through Grant ATM-9118963.

APPENDIX A

Details of the Numerical Solution

The solution of the balanced Ψ,Φ equation set used here is quite similar to that found in Davis and Emanuel (1991, hereafter referred to as DE). With moderate forcing, either one of these equations is readily solved using a standard method such as successive over-relaxation (SOR). Solving the system as a whole, however, proves to be much more difficult. The application of this balance model to the MCS regime is aggravated by the extremely large shears and strong temperature gradients (and hence large PV gradients) generated locally by the deep convection. While, at least in principle, a balanced solution exists to this PV distribution, the nonlinear terms are so dominant that success in achieving convergence with the numerical method becomes very dependent on the initial guess. The initial nonlinear error often forces the solution out of its attractor basin within the first cycle.

For times when strong convection was not present, an adequate initial guess was simply the primitive equation solution interpolated onto the analysis grid. When deep convection was present, the initial guess consisted of a combination of the balanced solution at an earlier time and the PE solution at the current time while boundary conditions were derived (by necessity) entirely from the current PE solution. During periods where domainwide diurnal temperature changes were occurring, this method was applied only to the streamfunction since the geopotential was systematically changing over large areas. At some times an additional nine point Gaussian smoothing of the initial guess fields was required to achieve convergence.

In addition to the carefully constructed initial guess discussed above, a few other adjustments were necessary to ensure convergence. During the first few cycles

of the inversion process, unstable lapse rates ($\partial^2\Phi/\partial\pi^2 < 0$) would occasionally appear as the geopotential made relatively large adjustments to a balanced state, creating a numerical instability. When this occurred, the static stability was set to a very small positive value. As the solver converged to a balanced Φ solution this problem disappeared.

Another consequence inherent in the solution of this inversion problem is a ''ringing'' as the system approaches convergence and oscillates between two solutions. This oscillation is damped by using an underrelaxation method after each cycle. Underrelaxation after the first few cycles was also useful in dampening out the positive feedback runaway behavior due to the initial guess error. Iversen and Nordeng (1984) found a comparable behavior with their family of balanced prognostic models. DE reported using a similar damping method in their diagnostic system.

Appropriate boundary conditions are an essential part of the PV inversion (Hoskins et al. 1985). Balanced model simulations are often formulated such that the boundary conditions are simple to apply. When inverting observed or PE model-generated data, the specification of boundary conditions can be much more difficult.

Boundary conditions as described in DE were used for the PV inversion with Ψ and Φ from the PE simulation specified on lateral boundaries. The same approach was used for horizontal (top and bottom) boundary conditions for Ψ. A Neumann horizontal boundary condition was used for Φ, namely $\partial\Phi/\partial\pi = -\theta$, with θ on these boundaries specified from the PE model results. For the χ, ω solver, boundary conditions consistent with the PE model are somewhat harder to derive since a relationship similar to (2.4) in DE does not exist for the divergent wind. In general, to maintain mass continuity in a domainwide sense, some divergent wind is required at each level. A boundary condition of $\chi = 0$ at the lateral boundaries was used for these calculations. This boundary condition has the effect of eliminating any tangential component of the divergent wind field along the boundaries. This side effect was found to be negligible when interpreting the results in the interior of the domain.

The upper and lower horizontal boundaries present more of a problem. The upper boundary is above 100 mb, well into the lower stratosphere. Due to the very stable nature of the stratosphere, it is reasonable to assume that most of the vertical motion seen there is due to gravity waves, and a rigid lid ($\omega=0$) is justified. The bottom of the analysis domain (a constant pressure surface) is *not* the earth's surface and boundary condition of $\omega=0$ is *not* justified here. Indeed, a significant amount of the convergence feeding the convective updrafts is found very near the surface where the high θ_e values are found. To derive $\omega(x,y)$ at the lower boundary, (6) was integrated downward using $\omega_{top} = 0$ and the two-dimensional divergence obtained from the PE model. This divergence was also used as the first guess in the cyclic-iteration procedure.

A much more detailed discussion of the solution technique can be found in Olsson (1994).

APPENDIX B

The Analysis Grid

The analysis grid corresponds to a subvolume of the model grid 2 (see Fig. 1, Part I, for locations of the model grids). To obtain this subvolume, the lateral boundary points of grid 2 were discarded, and to avoid possible nonphysical noise due to the upper boundary, the top five model levels were discarded. As the diagnostic system assumes frictionless flow, it would also be desirable to eliminate points in the boundary layer since friction effects are generally most significant near the surface. The boundary layer in this simulation was, at times, several kilometers deep. As a compromise, the bottom three model levels of grid 2 were also discarded.

Once this subset of model data was obtained for each analysis time (23/1800 to 24/1200 at 30-min intervals, all times UTC), the bottom level at each time was searched to find the minimum π value, and the top level was searched for the maximum π level. This defined the range of π (π_b and π_t, respectively) common to all grid columns in the model volume (x,y,σ_z) subset, and determined the bottom and top of the analysis (x,y,π) domain. With π_b and π_t determined, a clamped cubic spline $z \rightarrow \pi$ interpolation (Burden et al. 1981) of each field in the dataset was performed on each vertical column to place the model data on 16 evenly spaced constant-π surfaces. The model grid 2 horizontal grid spacing (Part I) was retained. The result was an analysis domain, 78 points E–W and 63 points N–S, with a horizontal spacing of 25 km, and 16 π levels, ranging from $\pi_b = 963$ J K^{-1} kg^{-1} to $\pi_t = 500$ J K^{-1} kg^{-1}, separated by a constant $\Delta\pi$ of 30.87 J K^{-1} kg^{-1}. Table 2 lists the π levels, their millibar equivalents and a representative geometric height for each level, which was taken from a point near the center of the storm region at 23/1800.

The highest terrain and hence the lowest π on the $\sigma_z = 4$ level of grid 2 is found along the western boundary and in the Appalachian, Ozark, and Smoky Mountains. Southern Iowa and northern Missouri, the region over which the storm occurred, has significantly lower terrain, making the bottom of the analysis domain well ($\sim$ 1 km) above the surface in the region of greatest interest and mitigating surface frictional effects ignored in the balanced analysis.

APPENDIX C

Local Variation of c_n

Within the region of a warm-core vortex with its large PV, the static stability is typically greater than that of the surrounding environment (Raymond and Jiang

1990). In the present case, the Brunt–Väisälä frequency, N, defined by

$$N^2 = g\frac{\partial \ln\theta}{\partial z} = \frac{g}{T}\left(\frac{dT}{dz} + \Gamma_d\right), \qquad \text{(C1)}$$

has been increased in the MCV by about 30% over the surrounding environment. Here, Γ_d in (C1) represents the dry adiabatic lapse rate and T the environmental temperature. Since the phase speed $c_n \propto N$, from (19) or (20) one might expect a dilatation of λ_R in the region of enhanced static stability due to a locally larger c_n there.

Moisture saturation is another factor effecting the static stability. For a saturated parcel displaced vertically, latent heating (cooling) partially compensates the temperature change due to adiabatic expansion(compression). Since a saturated parcel (ignoring precipitation effects) conserves equivalent potential temperature, θ_e, rather than θ, a moist Brunt–Väisälä frequency, N_m, given by

$$N_m^2 = g\frac{\partial \ln\theta_g}{\partial z} = \frac{g}{T}\left(\frac{dT}{dz} + \Gamma_m\right), \qquad \text{(C2)}$$

with Γ_m the saturated (with respect to water) adiabatic lapse rate, is obtained (Durran and Klemp 1982). Comparison of (C1) and (C2) shows that the difference between N and N_m is due the differing values of Γ_d and $\Gamma_m(T,p)$, the latter ranging from about 3.75 K gpkm^{-1} to the dry adiabatic value, 9.76 K gpkm^{-1} in the troposphere (Iribarne and Godson 1981). This saturated adiabatic effect, by decreasing c_n compared to that in an unsaturated atmosphere, would act to decrease λ_R. Chen and Frank (1993), in a numerical study of idealized MCVs, found significant contraction of λ_R when using N_m rather than N in their calculations.

In the present case, we found that these two effects largely cancelled, and our calculations of c_n for the storm-perturbed region did not differ significantly from the larger-scale value. For this reason, and due to the approximate scaling nature of λ_R, the larger-scale values for c_n are used here.

REFERENCES

Bretherton, C. S., and P. K. Smolarkiewicz, 1989: Gravity waves, compensating subsidence, and detrainment around cumulus clouds. *J. Atmos. Sci.,* **46,** 740–759.

Burden, R. L., D. J. Faires, and A. C. Reynolds, 1981: *Numerical Analysis.* Prindle, Weber & Schmidt, 598 pp.

Charney, J. G., 1948: On the scale of atmospheric motions. *Geofys. Publ.,* **17,** 1–17.

——, and M. F. Stern, 1962: On the stability of internal baroclinic jets in a rotating atmosphere. *J. Atmos. Sci.,* **19,** 159–172.

Chen, S. S., and W. M. Frank, 1993: A numerical study of the genesis of extratropical convective mesovortices. Part I: Evolution and dynamics. *J. Atmos. Sci.,* **50,** 2401–2426.

Cotton, W. R., M.-S. Lin, R. L. McAnelly, and C. J. Tremback, 1989: A composite model of mesoscale convective complexes. *Mon. Wea. Rev.,* **117,** 765–783.

Cram, J. M., R. A. Pielke, and W. R. Cotton, 1992: Numerical simulation of an analysis of a prefrontal squall line. Part II: Propagation of the squall line as an internal gravity wave. *J. Atmos. Sci.,* **49,** 209–225.

Crook, N. A., 1987: Moist convection at a surface cold front. *J. Atmos. Sci.,* **44,** 3469–3494.

——, R. E. Carbone, M. W. Moncreiff, and J. W. Conway, 1990: The generation and propagation of a nocturnal squall line. Part II: Numerical simulations, *Mon. Wea. Rev.,* **118,** 50–65.

Davis, C. A., and K. A. Emanuel, 1991: Potential vorticity diagnostics of cyclogenesis. *Mon. Wea. Rev.,* **119,** 1929–1953.

——, and M. L. Weisman, 1994: Balanced dynamics of mesoscale vortices in simulated convective systems. *J. Atmos. Sci.,* **51,** 2005–2030.

Durran, D. R., and J. B. Klemp, 1982: On the effects of moisture on the Brunt–Väisälä frequency. *J. Atmos. Sci.,* **39,** 2152–2158.

Emanuel, K. A., 1983: Elementary aspects of the interaction between cumulus convection and the large-scale environment. *Mesoscale Meteorology: Theories, Observation and Models,* D. K. Lilly and T. Gal-Chen, Eds., D. Riedel, 551–575.

Frank, W. M., 1983: The cumulus parameterization problem. *Mon. Wea. Rev.,* **111,** 1859–1871.

Fritsch, J. M., J. D. Murphy, and J. S. Kain, 1994: Warm core vortex amplification over land. *J. Atmos. Sci.,* **51,** 1780–1807.

Gill, A. E., 1982: *Atmosphere–Ocean Dynamics.* Academic Press, 662 pp.

Hack, J. J., and W. H. Schubert, 1986: Nonlinear response of atmospheric vortices to heating by organized cumulus convection. *J. Atmos. Sci.,* **43,** 1559–1573.

Haltiner, G. J., and R. T. Williams, 1980: *Numerical Prediction and Dynamic Meteorology.* 2d ed. Wiley and Sons, 477 pp.

Hertenstein, R. F. A., 1996: Evolution of potential vorticity associated with mesoscale convective systems. Dept. of Atmos. Sci. Paper 599, 177 pp. [Available from Department of Atmospheric Science, Colorado State University, Fort Collins, CO 80523-1371.]

——, and W. H. Schubert, 1991: Potential vorticity anomalies associated with squall lines. *Mon. Wea. Rev.,* **119,** 1663–1672.

Holton, J. R., 1992: *An Introduction to Dynamic Meteorology.* Academic Press, 507 pp.

Hoskins, B. J., M. E. McIntyre, and A. W. Robertson, 1985: On the use and significance of isentropic potential vorticity maps. *Quart. J. Roy. Meteor. Soc.,* **111,** 877–946.

Houze, R. A., Jr., 1989: Observed structure of mesoscale convective systems and implications for large scale heating. *Quart. J. Roy. Meteor. Soc.,* **115,** 425–461.

Iribarne, J. V., and W. L. Godson, 1981: *Atmospheric Thermodynamics.* D. Reidel, 259 pp.

Iversen, T., and T. E. Nordeng, 1984: A hierarchy of nonlinear filtered models-numerical solutions. *Mon. Wea. Rev.,* **112,** 2048–2059.

Jiang, H., and D. J. Raymond, 1995: Simulation of a mature mesoscale convective system using a nonlinear balance model. *J. Atmos. Sci.,* **52,** 161–175.

Johnson, R. H., and D. L. Bartels, 1992: Circulations associated with a mature-to-decaying midlatitude mesoscale convective system. Part II: Upper-level features. *Mon. Wea. Rev.,* **120,** 1301–1320.

Mapes, B. E., 1993: Gregarious tropical convection. *J. Atmos. Sci.,* **50,** 2026–2037.

McAnelly, R. L., and W. R. Cotton, 1986: Meso-β scale characteristics of an episode of meso-α scale convective complexes. *Mon. Wea. Rev.,* **114,** 1740–1770.

——, and ——, 1989: The precipitation lifecycle of mesoscale convective complexes over the central United States. *Mon. Wea. Rev.,* **117,** 784–808.

McWilliams, J. C., 1985: A uniformly valid model spanning the regimes of geostrophic and isotropic, stratified turbulence: Balanced turbulence. *J. Atmos. Sci.,* **42,** 1773–1774.

——, and P. R. Gent, 1980: Intermediate models of planetary circulations in the atmosphere and ocean. *J. Atmos. Sci.,* **37,** 1657–1678.

Nicholls, M.E., R. A. Pielke, and W. R. Cotton, 1991: Thermally

forced gravity waves in an atmosphere at rest. *J. Atmos. Sci.*, **48,** 2561–2572.

Olsson, P. Q., 1994: Evolution of balanced flow in a simulated mesoscale convective complex. Dept. of Atmos. Sci. Paper 570, 177 pp. [Available from Department of Atmospheric Science, Colorado State University, Fort Collins, CO 80523-1371.]

——, and W. R. Cotton, 1997: Balanced and unbalanced circulations in a primitive equation simulation of a midlatitude MCC. Part I: The numerical simulation. *J. Atmos. Sci.,* **54,** 457–478.

Ooyama, K., 1982: Conceptual evolution of the theory and modeling of the tropical cyclone. *J. Meteor. Soc. Japan,* **60,** 369–380.

Raymond, D. J., 1992: Nonlinear balance and potential vorticity thinking at large Rossby number. *Quart. J. Roy. Meteor. Soc.*, **118,** 987–1015.

——, and H. Jiang, 1990: A theory for long-lived mesoscale convective systems. *J. Atmos. Sci.,* **47,** 3067–3077.

Schubert, W. H, and J. J. Hack, 1982: Inertial stability and tropical cyclone development. *J. Atmos. Sci.,* **39,** 1687–1697.

——, ——, P. L. Silva Diaz, and S. R. Fulton, 1980: Geostrophic adjustment in an axisymmetric vortex. *J. Atmos. Sci.*, **37,** 1464–1484.

——, S. R. Fulton, and R. F. A. Hertenstein, 1989: Balanced atmospheric response to squall lines. *J. Atmos. Sci.,* **46,** 2478–2483.

Schmidt, J. M., and W. R. Cotton, 1990: Interactions between upper and lower tropospheric gravity waves on squall line structure and maintenance. *J. Atmos. Sci.,* **47,** 1205–1222.

Skamarock, W. C., M. L. Weisman, and J. B. Klemp, 1994: Three-dimensional evolution of simulated long-lived squall lines. *J. Atmos. Sci.*, **51,** 2563–2584.

Tripoli, G., and W. R. Cotton, 1989: A numerical study of an observed orogenic mesoscale convective system. Part II: Analysis of governing dynamics. *Mon. Wea. Rev.,* **117,** 301–324.

Zhang, D.-L., and J. M. Fritsch, 1988a: Numerical sensitivity of varying model physics on the structure evolution and dynamics of two mesoscale convective systems. *J. Atmos. Sci.*, **45,** 261–293.

——, and ——, 1988b: Numerical simulation of the meso-β structure and evolution of the 1977 Johnstown flood. Part III: Internal gravity waves and the squall line. *J. Atmos. Sci.,* **45,** 1252–1268.